



# Experimental validation of a phase-field model for fracture

K. H. Pham · K. Ravi-Chandar · C. M. Landis

Received: 18 July 2016 / Accepted: 5 January 2017 / Published online: 31 January 2017  
© Springer Science+Business Media Dordrecht 2017

**Abstract** Simulations from a numerical implementation of the phase-field model for brittle fracture are compared against analytical and experimental results in order to explore the verification and validation of the method. It is found that while the intrinsic length scale associated with the phase-field model can be set arbitrarily, the scale of the fracture process zone, and the scale at which the elastic field attains the corresponding analytical brittle fracture limit could be substantially larger than this intrinsic length. It is demonstrated that with a suitable choice of this length scale, phase-field simulations can provide valid predictions of the growth of cracks in quasi-static brittle fracture.

**Keywords** Crack initiation · Crack path · Cohesive zone · Polymethylmethacrylate · crack interaction

## 1 Introduction

The phase-field method is a versatile technique for solving problems of moving interfaces such as the formation of microstructures in solidification, multiphase flow, and image segmentation. In recent years, it has been applied to fracture mechanics in order to provide a remedy for the discontinuity of the displacement

field along the crack surface which poses difficulty for numerical solution techniques. There exist two kinds of phase-field formulations: the formulation based on Griffith's fracture theory (Bourdin et al. 2008) and the formulation based on Ginzburg-Landau theory (Karma et al. 2001). Ambati et al. (2015) provide a detailed comparative review of different formulations of phase-field models. While our ultimate aim is to use the phase-field formulation to investigate the onset and growth of crack front fragmentation under mixed-mode I + III, here we limit our effort to the verification and validation of the method under in-plane modes I + II. The phase-field formulation based on Griffith's fracture theory is reviewed briefly in Sect. 2 to provide the context for the simulations in the following sections. Numerical implementation is briefly discussed in Sect. 3. The restrictions on the length scales associated with the phase-field simulation are explored in Sect. 4 through comparison of the numerical results to exact analytical solutions. Finally, validation of the numerical simulations is demonstrated in Sect. 5 through comparison to experiments performed under mode I and mixed modes I + II loading conditions.

## 2 A review of a phase-field model of Griffith theory of fracture

Consider a solid body enclosed in the domain  $\Omega$  with the boundary  $\partial\Omega$  and a crack  $\Gamma$  (shown in Fig. 1). The domain boundary  $\partial\Omega$  is divided into

K. H. Pham · K. Ravi-Chandar (✉) · C. M. Landis  
Center for Mechanics of Solids, Structures and Materials,  
Department of Aerospace Engineering and Engineering  
Mechanics, The University of Texas at Austin, Austin,  
TX 78712-0235, USA  
e-mail: ravi@utexas.edu

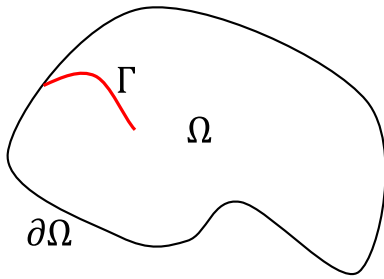


**Fig. 1** A sketch of a solid body with a crack

two non-overlapping subsets  $\partial\Omega_h$  where the tractions are prescribed, and  $\partial\Omega_g$  where the displacements are prescribed. According to the Griffith theory of fracture, the solution to a static crack growth problem is governed by the minimization of the energy functional:

$$\Psi = \int_{\Omega} \psi_e d\Omega + \int_{\Gamma} G_c d\Gamma \quad (1)$$

where  $\psi_e$  and  $G_c$  are strain energy density and fracture energy, respectively. In the phase-field formulation, the fracture surface is approximated by a phase-field  $c(\mathbf{x})$ ,  $c \in [0, 1]$ , which represents the material state:  $c = 0$  indicates that the material is fully damaged, while the material is intact for  $c = 1$ . [Bourdin et al. \(2008\)](#) and [Miehe et al. \(2010\)](#) used the following approximation for the energy associated with the fracture, first introduced by [Bourdin et al. \(2000\)](#):

$$\int_{\Gamma} G_c d\Gamma \sim \int_{\Omega} G_c \left[ \frac{(c - 1)^2}{4l_0} + l_0 \frac{\partial c}{\partial x_i} \frac{\partial c}{\partial x_i} \right] d\Omega \quad (2)$$

where  $l_0$  is an intrinsic length scale. The above phase-field approximation allows the surface integral term to be approximated through a volume integral and, the energy functional becomes:

$$\Psi_0 = \int_{\Omega} \psi_e d\Omega + \int_{\Omega} G_c \left[ \frac{(c - 1)^2}{4l_0} + l_0 \frac{\partial c}{\partial x_i} \frac{\partial c}{\partial x_i} \right] d\Omega \quad (3)$$

While  $\Psi$  and  $\Psi_0$  are not equal, it has been shown ([Chambolle 2004, 2005](#)), following the ideas of [Ambrosio and Tortorelli \(1990, 1992\)](#), that  $\Psi_0$  approaches  $\Psi$

in the sense of  $\Gamma$ -convergence as  $l_0 \rightarrow 0$ . The governing Euler-Lagrange equations are derived from Eq. (3) as:

$$\begin{cases} \frac{\partial \sigma_{ij}}{\partial x_j} = 0 & \text{in } \Omega \\ \frac{l_0}{2G_c} \frac{\partial \psi_e}{\partial c} + \frac{c-1}{4} - l_0^2 \frac{\partial^2 c}{\partial x_j \partial x_j} = 0 & \text{in } \Omega \end{cases} \quad (4)$$

$$\text{where } \sigma_{ij} = \frac{\partial \psi_e}{\partial \varepsilon_{ij}}$$

These equations are subjected to the boundary conditions:

$$\begin{cases} \mathbf{u} = \mathbf{g} & \text{on } \partial\Omega_g \\ \boldsymbol{\sigma} \cdot \mathbf{n} = \mathbf{h} & \text{on } \partial\Omega_h \\ \nabla c \cdot \mathbf{n} = 0 & \text{on } \partial\Omega \end{cases} \quad (5)$$

The material softening due to the presence of a crack can be enforced by the quadratic degradation function introduced by [Bourdin et al. \(2000\)](#) in the context of fracture and by Ambrosio and Tortelli ([1992](#)) in the context of image processing:

$$\psi_e := c^2 \psi_e \quad (6)$$

More general types of degradation of energy have been considered by [Braides \(1998\)](#), and studied in detail by [Pham et al. \(2011a,b\)](#). Here, we follow [Borden et al. \(2012\)](#), and write a more general material degradation function  $g(c)$  as:

$$\psi_e := g(c) \psi_e(\boldsymbol{\varepsilon}) \quad (7)$$

[Borden et al. \(2012\)](#) suggested a cubic degradation of the form:

$$g(c) = s \left( c^3 - c^2 \right) + 3c^2 - 2c^3 \quad (8)$$

which, with  $s > 0$  and small provides a linear stress-strain response prior to the onset of damage. A significant limitation of the model represented in Eq. (6) (Bourdin's model) is that it allows a crack to grow under compressive loading condition. In order to suppress this nonphysical behavior, [Amor et al. \(2009\)](#) presented a model in which material softening based on the decomposition of the strain energy density into “positive”  $\psi_e^+$  and “negative”  $\psi_e^-$  parts was considered corresponding to the dilatational and deviatoric parts of the strain tensor; [Miehe et al. \(2010\)](#) used an alternative model where

the strain tensor is decomposed into positive and negative parts (a somewhat similar was model presented by Ortiz 1985):

$$\boldsymbol{\varepsilon} = \frac{1}{2} (\nabla \mathbf{u} + \nabla^T \mathbf{u}) = \boldsymbol{\varepsilon}_+ + \boldsymbol{\varepsilon}_-$$

$$\boldsymbol{\varepsilon}_+ := \sum_{i=1}^{nsd} \langle \varepsilon_i \rangle_+ \mathbf{n}_i \otimes \mathbf{n}_i \quad \text{and} \quad \boldsymbol{\varepsilon}_- := \sum_{i=1}^{nsd} \langle \varepsilon_i \rangle_- \mathbf{n}_i \otimes \mathbf{n}_i \quad (9)$$

where  $\varepsilon_i$  are the principal strains and  $\mathbf{n}_i$  ( $i = 1 - nsd$ ,  $nsd$  is the number of space dimensions) are the principal strain directions; the operators  $\langle \cdot \rangle_+$ ,  $\langle \cdot \rangle_-$  are defined as  $\langle x \rangle_+ = 1/2(x + |x|)$ ,  $\langle x \rangle_- = 1/2(x - |x|)$ . Strain energies  $\psi_e^+$ ,  $\psi_e^-$  computed from the positive and negative components, respectively, of the strain tensor are written as:

$$\psi_e^+(\boldsymbol{\varepsilon}) = \frac{\lambda}{2} \langle \operatorname{tr}(\boldsymbol{\varepsilon}) \rangle_+^2 + \mu \operatorname{tr}(\boldsymbol{\varepsilon}_+^2)$$

$$\psi_e^-(\boldsymbol{\varepsilon}) = \frac{\lambda}{2} \langle \operatorname{tr}(\boldsymbol{\varepsilon}) \rangle_-^2 + \mu \operatorname{tr}(\boldsymbol{\varepsilon}_-^2) \quad (10)$$

where  $\lambda$  and  $\mu$  are the Lamé constants. The degradation function is applied only to the “positive” part of the strain energy density to prohibit the crack from evolving under compressive loading:

$$\psi_e := g(c) \psi_e^+ + \psi_e^- \quad (11)$$

In order to prevent the crack from healing, additional equality (Bourdin 1999) or inequality (Giacomini 2005) constraints on the phase field evolution have been used. Miehe et al. (2010) enforced the irreversibility condition, through a strain-history field:  $\mathcal{H}_0 = \mathcal{H}(\mathbf{x}, t_0) = 0$  at the initial step  $t = t_0$ ,  $\mathcal{H} = \mathcal{H}(\mathbf{x}, t_n)$  at the loading step  $t = t_n$ . Borden et al. (2012) also used the initial strain-history field  $\mathcal{H}_0$  to model the initial crack. Here, we will follow the Miehe formulation. The strain-history field for Bourdin’s model can be written as:

$$\mathcal{H}(\mathbf{x}, t_n) = \begin{cases} \psi_e, & \text{for } \psi_e > \mathcal{H}(\mathbf{x}, t_{n-1}) \\ \mathcal{H}(\mathbf{x}, t_{n-1}), & \text{otherwise} \end{cases} \quad (12)$$

And for Miehe’s model:

$$\mathcal{H}(\mathbf{x}, t_n) = \begin{cases} \psi_e^+, & \text{for } \psi_e^+ > \mathcal{H}(\mathbf{x}, t_{n-1}) \\ \mathcal{H}(\mathbf{x}, t_{n-1}), & \text{otherwise} \end{cases} \quad (13)$$

Substituting the strain-history field and material degradation model into the system of Eq. (4) yields:

$$\begin{cases} \frac{\partial \sigma_{ij}}{\partial x_j} = 0 & \text{in } \Omega \\ Q(c) - l_0^2 \frac{\partial^2 c}{\partial x_j \partial x_j} = 0 & \text{in } \Omega \end{cases} \quad (14)$$

$$\text{where } Q(c) = \frac{l_0 \mathcal{H} g'(c)}{2G_c} + \frac{c-1}{4},$$

$$\sigma_{ij} = \begin{cases} g(c) \frac{\partial \psi_e}{\partial \varepsilon_{ij}}, & \text{for Bourdin's model} \\ g(c) \frac{\partial \psi_e^+}{\partial \varepsilon_{ij}} + \frac{\partial \psi_e^-}{\partial \varepsilon_{ij}}, & \text{for Miehe's model} \end{cases}$$

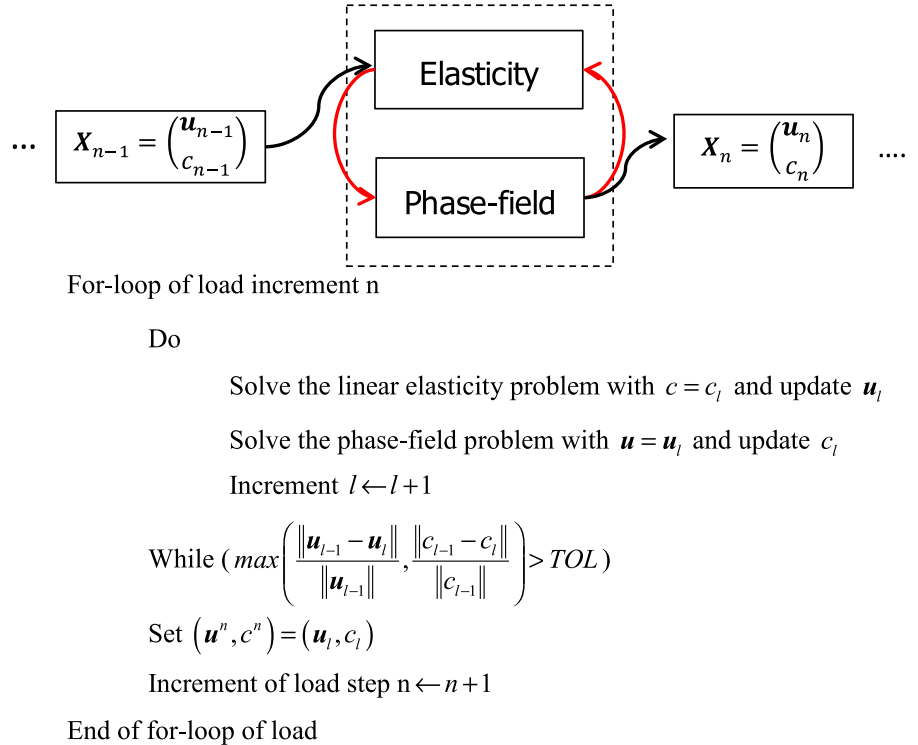
The governing equations (14) are coupled between the displacement field and phase-field and can be solved with a coupled formulation or operator splitting schemes. Bourdin (1999) and Bourdin et al. (2000) showed that  $\Psi_0$  is separately convex in the  $\mathbf{u}$  and  $c$ , leading to the alternate minimization technique illustrated in Fig. 2.

The phase-field model approach offers an attractive path for modeling crack propagation. However, the choice of the intrinsic length scale  $l_0$ , and the validation for the phase field model need to be considered carefully. Many of the works on phase-field models have compared their results on mode I loading for the single edge notch geometry or mode II loading for a shear loading geometry. Some have addressed more complex crack path evolution problems. However, most of the comparisons with the experimental data were performed qualitatively. In this work we have performed carefully designed experiments to provide quantitative data for the validation of the phase-field and then examined the quantitative correspondence between the global load-displacement response as well as the corresponding crack path evolution.

### 3 Numerical implementation of the phase-field model

We developed a fully three-dimensional finite element code for the phase-field formulation discussed in Sect. 2. The following ingredients of the phase-field model were considered in our implementation: both Bourdin’s and Miehe’s models for material softening were implemented (Miehe’s model is assumed for all the simulations reported in the following sections, unless stated otherwise); the strain history field

**Fig. 2** Quasi-static splitting scheme for decoupling the system of elasticity and phase-field PDEs



(Miehe et al. 2010) was used to enforce the irreversibility condition for phase-field parameter. This code was written on a parallel framework using Message Passing Interface library (MPI), Metis library (Karypis and Kumar 1999) for mesh partition and Petsc (Balay et al. 2014) for nonlinear/linear solvers. The displacement field and phase-field equations are solved based on a staggered scheme with iteration within each load step. However, for deciding on convergence, instead of using the displacement or phase-field based measures indicated in Fig. 2, we adopted the energy functional convergence measure as discussed in Ambati et al. (2015):

$$\alpha = \frac{\Psi_{n-1} - \Psi_n}{\Psi_n} < tol \quad (15)$$

where  $\Psi_n, \Psi_{n-1}$  are the energy functional for the current and previous load steps. For the simulations reported in this section, the tolerance was set to  $tol = 10^{-7}$ ; it took about 500 iterations between the phase-field and displacement field equations to attain convergence. Post-processing was accomplished with ParaView and special MATLAB codes. All simulations were performed at the Texas Advanced Computing Center's Stampede Supercomputer; depending on problem size, 16–256 cores were used. Typical run

times were on the order of 1–10 h, depending on the problem size.

The elastic material properties,  $(E, \nu)$ , the modulus of elasticity and Poisson's ratio, respectively, are taken from experimental calibration data as appropriate. For the fracture energy, Bourdin et al. (2008) showed that the fracture energy is amplified in the simulation based on finite element discretization and that this has to be taken into account in formulating the simulation. Therefore, we scaled the fracture energy used in the simulation by the approximation proposed by Bourdin et al. (2008):

$$G_c^{sim} = \frac{G_c}{(1 + h/4l_0)} \quad (16)$$

where  $G_c$  is the actual material fracture energy, and  $h$  is the minimum size of the mesh; this leaves the intrinsic scale in the phase-field model  $l_0$  yet to be chosen. One option is to let this be unspecified and all lengths are then scaled by the value of  $l_0$ . Another option is to obtain an estimate of  $l_0$  by considering the response of the phase-field model to homogenous uniaxial deformation (see Borden et al. 2012); for the quadratic degradation function this solution indicates that the stress attains a peak value of

$$\sigma_c = \frac{9}{16} \sqrt{\frac{E' G_c}{6l_0}} \quad (17)$$

when the phase-field parameter reaches  $c_c = 3/4$ . Note that  $E' = E/(1 - \nu^2)$ ; corresponding to this, the strain level is  $\varepsilon_c = \sqrt{G_c/(6l_0 E')}$ . Rearranging, one can obtain the following estimate

$$\sigma_c^2 l_0 = \frac{27 E' G_c}{512} \quad (18)$$

This implies that corresponding to any chosen value of  $l_0$ , there is an appropriate peak stress  $\sigma_c$ . For a material with  $E = 2.98$  GPa,  $\nu = 0.35$ , and  $G_c = (1 - \nu^2) K_{IC}^2/E = 0.285$  kJ/m<sup>2</sup>, assuming that the peak stress is equivalent to the tensile strength of the material ( $\sigma_c \sim 50$  MPa) yields  $l_0 \sim 20 \times 10^{-6}$  m. Since this will result in a large number of degrees of freedom, particularly when we wish to simulate physical experiments with dimensions of many centimeters, we will take  $l_0 \sim 100 \times 10^{-6}$ , and compensate accordingly on  $\sigma_c$ . Therefore,  $E$ ,  $\nu$ ,  $G_c$ ,  $l_0$  are the primary parameters used in the phase-field simulations. In the following, we will use normalized values in some simulations, and physical values when simulations are to be compared to specific experiments.

#### 4 Verification by comparison to analytical solutions

While the phase-field model converges to the Griffith theory in the limit  $l_0 \rightarrow 0$ , it should be recognized that at a fixed value of  $l_0$ , the model resembles that of a damaging elastic material, and hence develops a damaged zone near the crack tip; this zone resembles a Dugdale–Barenblatt (DB) type cohesive zone in the vicinity of the crack tip. Therefore, it should be possible to develop a comparison between the analytical solution of the DB model and the phase field model for a crack in equilibrium. This is considered in Sect. 4.1 for a semi-infinite crack with a square-root singular field imposed at a distance  $R$  from the crack tip. This is followed in Sect. 4.2 by a comparison of the crack opening profile for a problem with a microcrack interacting with a macrocrack, a problem for which an exact two-dimensional elasticity solution was presented by Rubinstein (1985). Growth of cracks under mixed-mode loading is discussed in Sect. 4.3.

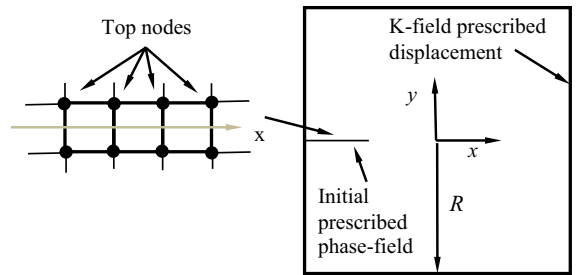


**Fig. 3** Geometry of the crack for the simulations with K-field displacement boundary conditions

##### 4.1 Semi-infinite crack with a Dugdale–Barenblatt cohesive zone

Consider a semi-infinite crack in an infinite plate, loaded in the far-field to generate a square-root singular stress field dictated by the opening mode stress intensity factor (SIF)  $K_I^\infty$ ; let a Dugdale–Barenblatt type cohesive zone form near the crack tip. Considering a *constant* cohesive stress  $\sigma_c$ , we get an estimate of the size of the cohesive zone as:

$$\alpha = \frac{\pi}{8} \left( \frac{K_I^\infty}{\sigma_c} \right)^2 \approx 7.5l_0 \quad (19)$$

where  $\sigma_c$  is the peak stress generated in the phase-field model. The phase-field simulation set-up is shown in Fig. 3. The domain of simulation is a square of size  $4000l_0 \times 4000l_0$ ; such a large domain is chosen in order to ensure that the displacement field associated with the asymptotic K-field of a crack whose tip is at the origin ( $x = 0, y = 0$ ) may be prescribed on the boundary of the domain:

$$\begin{cases} u_x(r, \theta) \\ u_y(r, \theta) \end{cases} = \frac{(1 + \nu) K_I^\infty}{2E} \left( \frac{r}{2\pi} \right)^{\frac{1}{2}} \times \begin{bmatrix} (2\kappa - 1) \cos(\frac{\theta}{2}) - \cos(\frac{3\theta}{2}) \\ (2\kappa + 1) \sin(\frac{\theta}{2}) - \sin(\frac{3\theta}{2}) \end{bmatrix} \quad (20)$$

where  $\kappa = 3 - 4\nu$  for plane strain. The computational mesh contains 50,000 hexahedral elements and it was generated in such a way that there is one line of elements with size  $h = l_0/2$  along the  $x$ -axis from  $x = -2000l_0$  to  $x = 10l_0$ . Two solution strategies were used: “growth solution” and “healing solution”. In the “growth solution” approach, the phase-field parameters of those elements which lie between  $x = -2000l_0$  to

$x = -1000l_0$  were prescribed to be zero. Then, we let this initial short crack to “grow” to its final length in the equilibrium state. In the “healing solution” approach, none of the nodes was prescribed in the phase-field solver, but we instead provided the initial guesses for the solutions to both phase-field and elasticity solvers. These initial solution guesses are associated with the displacement field and phase-field of the semi-infinite crack domain with the crack tip located at the origin. No irreversibility condition was imposed on the phase-field parameter in the “healing solution” approach. The two solution strategies provided the same crack opening profile after the staggered scheme was completed.

The equilibrium solution is obtained in the phase field simulations after about 500 iterations of the staggered scheme; the displacement in the  $y$  direction of the upper and lower nodes of the central line of elements were analyzed. Figure 4a, b show the comparison of the crack opening displacement (COD) from the phase-field solution (red dashed line for the quadratic degradation function and red dashed-dotted line for the cubic degradation function) with the analytical solution from the DB cohesive zone model (blue line) and the linear elastic K-field solution (black dashed line). The COD profile from the phase-field solution has features that are similar to the DB solution and approaches the K-field solution far away from the crack tip. The solution from phase-field model indicates a COD profile resembling a cohesive zone of the length  $\alpha \sim 8l_0$  for the quadratic degradation function and  $\alpha \sim 3l_0$  for the cubic degradation function, indicating differences from the DB estimate due to differences in the cohesive stress distribution. However, since the phase-field model is expected to be a solution to the elastic problem—meaning that the solution should match the elastic field—one raises the question of how far away from the crack tip the phase-field solution matches the elastic solution? From Fig. 4b it can be seen clearly that at a distance of about  $50l_0$ , there is still a significant difference between the phase-field solution and linear elastic solution. Figure 4c shows the deviation in the COD as a function of the distance from the crack tip; from this we see that the elastic field is approached to within 0.1% as long as one is  $500l_0$  away from the crack tip for both the quadratic and cubic degradation functions. Therefore, it appears that the disturbance in the stress field caused by introducing damage over a characteristic distance  $l_0$  perturbs the elastic field over

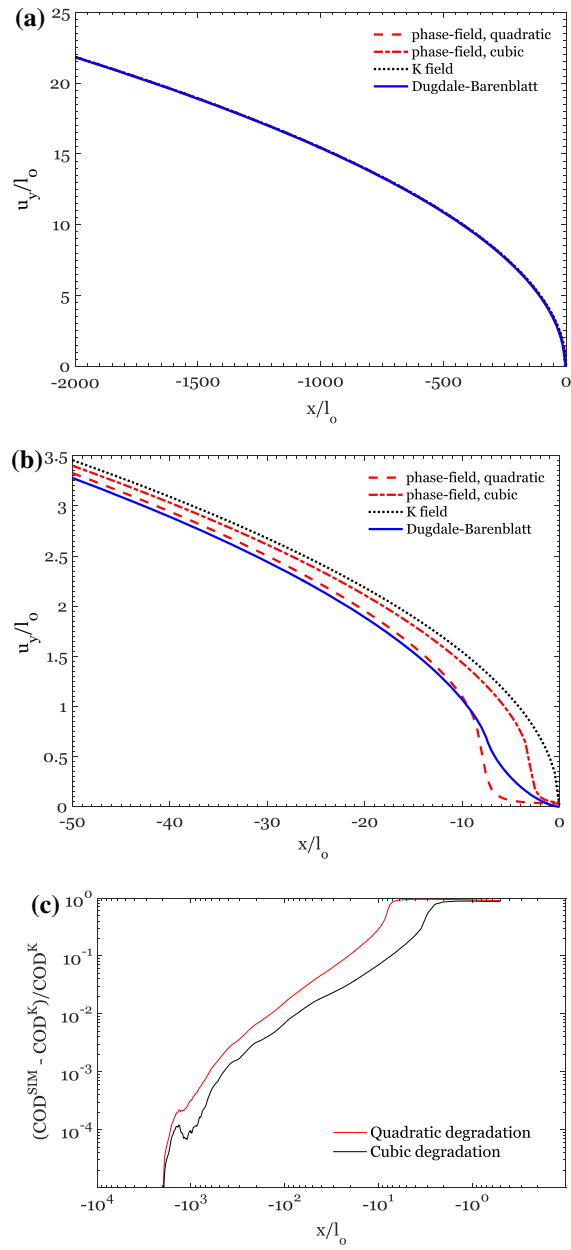


**Fig. 4** **a** Comparison of the crack opening profile behind the crack tip between phase-field solution, the linear elastic K-field solution and the Dugdale–Barenblatt model. **b** Comparison of the COD in a small region near the crack tip. **c** Difference in the COD between the phase-field solution (quadratic and cubic degradation function) and the elastic K-field solution; to drop this error below 0.1%, one needs to be  $\sim 630l_0$  away from the crack tip for the quadratic degradation, and about  $\sim 450l_0$  for the cubic degradation function

$500l_0$ . This is particularly important when interactions between cracks are to be considered, as illustrated in the next section.

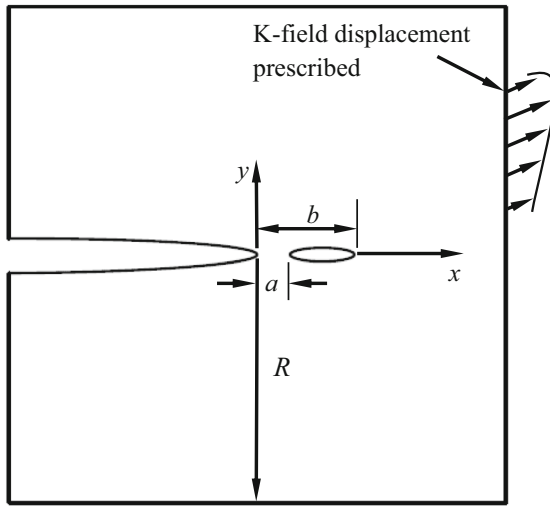


**Fig. 5** Rubinstein's problem set up:  $a = 500l_0$ ,  $b = 6a$ ,  $R = 10b$ , where  $l_0$  is the characteristic length used in the phase-field formulation. The displacement applied on the boundary is the mode I K-field displacement associated with the crack tip at  $(x = 0, y = 0)$  location with the mode I stress intensity factor  $K_I^\infty = K_{IC}/\gamma$  [see Eq. (20)]

#### 4.2 Macrocrack interaction with a microcrack

The second problem of verification that we consider relates to the interaction between cracks. Rubinstein (1985) considered a problem of the interaction of a collinear periodic array of microcracks ahead of a semi-infinite macrocrack and determined the SIFs both at the macrocrack and microcrack tips. For the special case of a single microcrack ahead of a macrocrack (see geometry in Fig. 5), the SIFs are given below<sup>1</sup>:

$$\begin{aligned} K_I(0) &= K_I^\infty \sqrt{\frac{b}{a}} \frac{E(1-a/b)}{K(1-a/b)} \\ K_I(a) &= K_I^\infty \left( \frac{b}{a} \frac{E(1-a/b)}{K(1-a/b)} - 1 \right) (b/a - 1)^{-1/2} \\ K_I(b) &= K_I^\infty \left( 1 - \frac{E(1-a/b)}{K(1-a/b)} \right) (1-a/b)^{-1/2} \end{aligned} \quad (21)$$

where  $K_I(0)$ ,  $K_I(a)$  and  $K_I(b)$  are the stress intensity factors at the macrocrack tip, left microcrack tip and right microcrack tip, respectively, and  $K_I^\infty$  is the stress intensity factor applied far-field from the macro-

micro-crack system. In addition, the displacement along the line  $y = 0$  was also calculated:

$$u_y(y=0) = \frac{\kappa+1}{2\mu} \frac{K_I^\infty}{2\sqrt{2\pi}} \times \text{Im} \left[ \int \frac{c-z}{\sqrt{z(a-z)(b-z)}} dz \right] \quad (22)$$

where  $z = x + iy$  and  $\mu$  is the shear modulus. Other elements of the stress field could also be determined with some additional effort, but this is not needed for the purposes of the comparison sought here. These SIFs at all crack tips are plotted in Fig. 6, normalized by the applied  $K_I^\infty$ . It is clear that the microcrack amplifies the SIF of the macrocrack. This amplification increases as the distance between the microcrack and macrocrack decreases. For example, the SIF at the macrocrack is enhanced 20% when the ratio  $a/(b-a) = 0.2$ . This means if one applies the far-field displacement associated with SIF which is 20% less than the material critical SIF  $K_{IC}$  on the boundary, the SIF at the macrocrack tip will reach  $K_{IC}$ ; and the macrocrack will grow with any further increase of the far-field displacement. We explore this problem using the phase-field simulation. The problem set-up is shown in Fig. 5. Next, we look into the different lengths associated with the problem in order to determine the appropriate discretization. Let  $l_0$  represent the intrinsic size scale for the gradient damage model in the phase-field simulation. Then, from the results in Sect. 4.1 concerning the semi-infinite crack problem,  $\alpha \sim 10l_0$  represents the cohesive zone size scale and sets the intrinsic scale for the fracture problem. From the geometry of the crack interaction problem,  $a$ , the separation distance between the macro and micro crack tips, sets the smallest geometric length scale and this should be large in comparison to  $\alpha$ , in order to recover the appropriate elastic solution. Based on the discussion in Sect. 4.1, we choose  $a \sim 50\alpha \sim 500l_0$ . Next, in order to enhance the SIF at the main crack tip by about 20%, we must select  $a/(b-a) \sim 0.2$  (based on Rubinstein 1985); this implies  $b = 6a = 300\alpha = 3000/l_0$ . The macro-crack K-field boundary condition must be applied at a distance  $R$  from the crack tip; this must be far enough that the displacement field corresponding to the K-field may be applied (and the applied  $K_I^\infty$  must be at least 20% below  $K_{IC}$ ). Note that we apply the K-field displacement for a single crack at the outer boundary, while the exact displacements from the analytical solutions supplied in Rubinstein (1985) are likely to be modified

<sup>1</sup> There was a minor typographical error in the formula for  $K_I(a)$  in Rubinstein (1985).

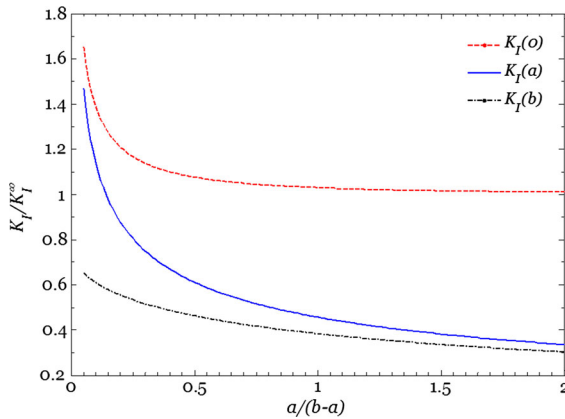


**Fig. 6** SIFs for Rubinstein's problem of the interaction of a semi-infinite macrocrack with a single microcrack

slightly by the presence of the microcrack at distances from the macrocrack tip that are small in relation to the size of the microcrack. Therefore, we shall require  $R \gg b$  and take  $R \sim 10b = 30,000l_0$ . Any error associated with this could be removed by applying the exact displacements from the Rubinstein (1985) solution. It is easy to see that even for simple problems, the discretization would yield large numbers of degrees of freedom. This problem will get exacerbated if the distance between the cracks decreases further: decreasing  $a$  will demand a commensurate reduction in  $l_0$ .

The microcrack is modeled by prescribing zero phase-field parameter for all the nodes located within the microcrack line as discussed in Sect. 4.1. Similarly, all the nodes located within the macrocrack line are provided with zero initial guesses (the “healing” solution approach was used in these simulations). The mesh contains 150,000 hexahedral elements. The displacements on the far boundary are prescribed with fixed values associated with  $K_I^\infty = K_{IC}/\gamma$ , centered at the macrocrack tip. With this loading setup, we determine where the crack will end up. For the case of  $\gamma = 1.2$  the macrocrack ends up at location  $x \sim -20l_0$ . If we increase the far-field displacement by setting  $\gamma = 1.19$ , the macrocrack is located at  $x \sim -8l_0$  corresponding to a sharp crack tip at the origin. This means the phase-field solution only gives the SIF amplification of the macrocrack 1% less than the closed-form solution of Rubinstein (1985). Figures 7 and 8 show a comparison of the phase-field solution for the crack opening displacement along the crack line associated with  $\gamma = 1.19$  and  $\gamma = 1.20$ , respectively, against

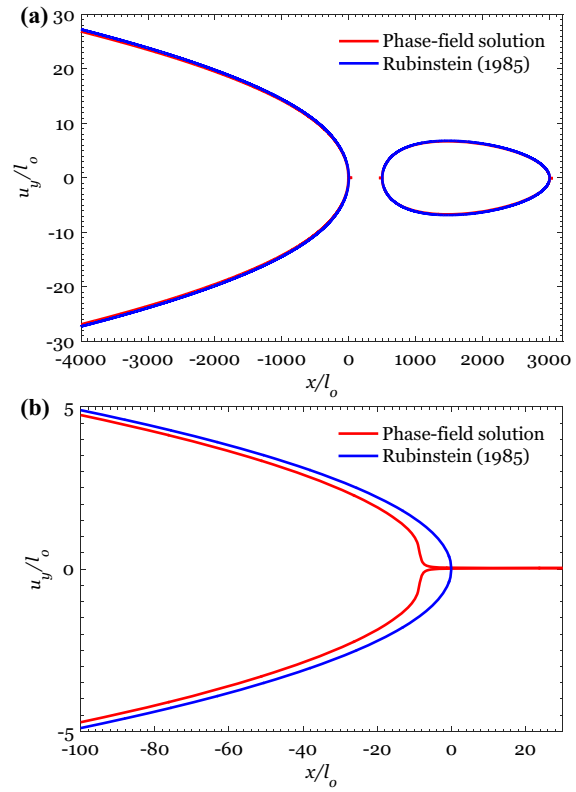


**Fig. 7** Comparison between the phase-field solution and Rubinstein's solution for the case of  $\gamma = 1.19$ : **a** crack opening profile of macrocrack and microcrack, **b** crack opening profile near the macrocrack tip

the closed-form solution of Rubinstein (1985). At distances from the crack tip that are greater than  $500l_0$ , the differences in the COD are less than 2%, indicating that the phase-field can provide acceptable solutions that are close to exact analytical solutions based on linear elasticity.

#### 4.3 Crack growth under mixed-mode I + II

In the two problems considered in Sects. 4.1 and 4.2, the cracks were stationary at the Griffith threshold. We now turn to verification of the code for crack growth under continued loading. Four problems are considered, one each for pure mode I and pure mode II and two for mixed modes I + II; in each case, a parallelepipedic region similar to the one shown in Fig. 3 is considered, with full three-dimensional discretization and K-field boundary conditions are imposed. A view of the discretization used near the crack tip is shown in Fig. 9a; as

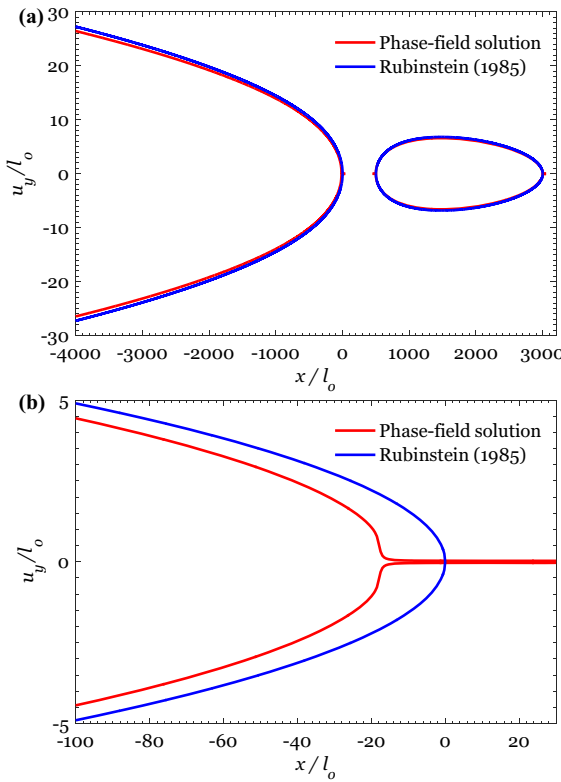


**Fig. 8** Comparison between the phase-field solution and Rubinstein’s solution for the case of  $\gamma = 1.2$ : **a** crack opening profile of macrocrack and microcrack, **b** crack opening profile near the macrocrack tip

in the previous examples, we set  $h = l_0/2$  in the region near the crack tip. The outer boundary at which the K-field displacements corresponding to modes I and II displacements were applied was set at  $R = 1000l_0$ ; as discussed earlier, this is adequate to recover the elastic solution at large distances from the local perturbations near the crack tip arising from the damage model. The mode I simulation was performed in a number of steps; Step 0 corresponds to applying a displacement field corresponding to  $K_I^\infty = K_{IC}$  and arriving at a converged solution from the staggered iteration scheme analogous to that in Sect. 4.1. For continued mode I loading, with increasing far-field  $K_I^\infty$  the phase-field model “grows” the opening mode crack straight ahead. We note that the phase-field solution obtained in Step 0 can be taken to correspond to a “natural” crack and used in further simulations of different modes of loading. Therefore for mode II and mixed-mode simulations, the phase-field solution from Step 0 of the mode I simulation is

taken as the initial value for the phase-field; mode II or mixed mode loading is then applied by prescribing the elastic K-field at the outer boundary; in Steps 1 through N, the far-field  $(K_I^\infty, K_H^\infty)$  was increased in small steps to grow the kinked opening mode crack. Note that no criterion for determination of the crack path is explicitly imposed in the phase field formulation, and that the crack must seek the direction along which the system attains a minimum potential energy. Figure 9b through 9e show the observed crack path under different mixed-mode loading conditions.

What is the expected response under mixed-mode I+II loading? There are different criteria that have been used in the last half-century. The three most commonly used criteria – the maximum tangential (or hoop) stress criterion (MTS), the principle of local symmetry (PLS) and the maximum energy release rate criterion (ERR) – are compared with the phase field simulations. These three criteria are summarized briefly. The MTS criterion (Erdogan and Sih 1963) postulates that a mixed-mode I+II crack would extend in the direction  $\gamma_c$  along which  $\partial\sigma_{\theta\theta}/\partial\theta = 0$ . This yields:

$$\gamma_c = 2 \tan^{-1} \left[ \frac{1 - \sqrt{1 + 8(K_H^c/K_I^c)^2}}{4K_H^c/K_I^c} \right], \text{ when } \cos^3 \left( \frac{\gamma_c}{2} \right) \left[ 1 - \frac{3K_H^c}{K_I^c} \tan \frac{\gamma_c}{2} \right] = \frac{K_{IC}}{K_I^c} \quad (23)$$

The evaluation of the other two criteria is quite difficult in general; both the PLS (Goldstein and Salganik 1974) and the ERR require the calculation of the stress intensity factor along kinked cracks; this has been calculated by Leblond (1999) using first order perturbation calculations: for a crack kinked at an angle  $\gamma$ , the stress intensity factors at the kinked crack tip in terms of the applied stress intensity factors are given as:

$$k_I(\gamma) = F_{I,I}(\gamma)K_I + F_{I,II}(\gamma)K_{II} \\ k_{II}(\gamma) = F_{II,I}(\gamma)K_I + F_{II,II}(\gamma)K_{II} \quad (24)$$

The functions  $F_{I,I}(\gamma)$ ,  $F_{I,II}(\gamma)$ ,  $F_{II,I}(\gamma)$ ,  $F_{II,II}(\gamma)$  are given in Leblond (1999). The PLS criterion asserts that the crack will grow in the direction in which the local mode II stress intensity factor is zero, establishing a locally opening mode crack:

$$k_I(\gamma_c) = K_{IC}, k_{II}(\gamma_c) = 0 \quad (25)$$

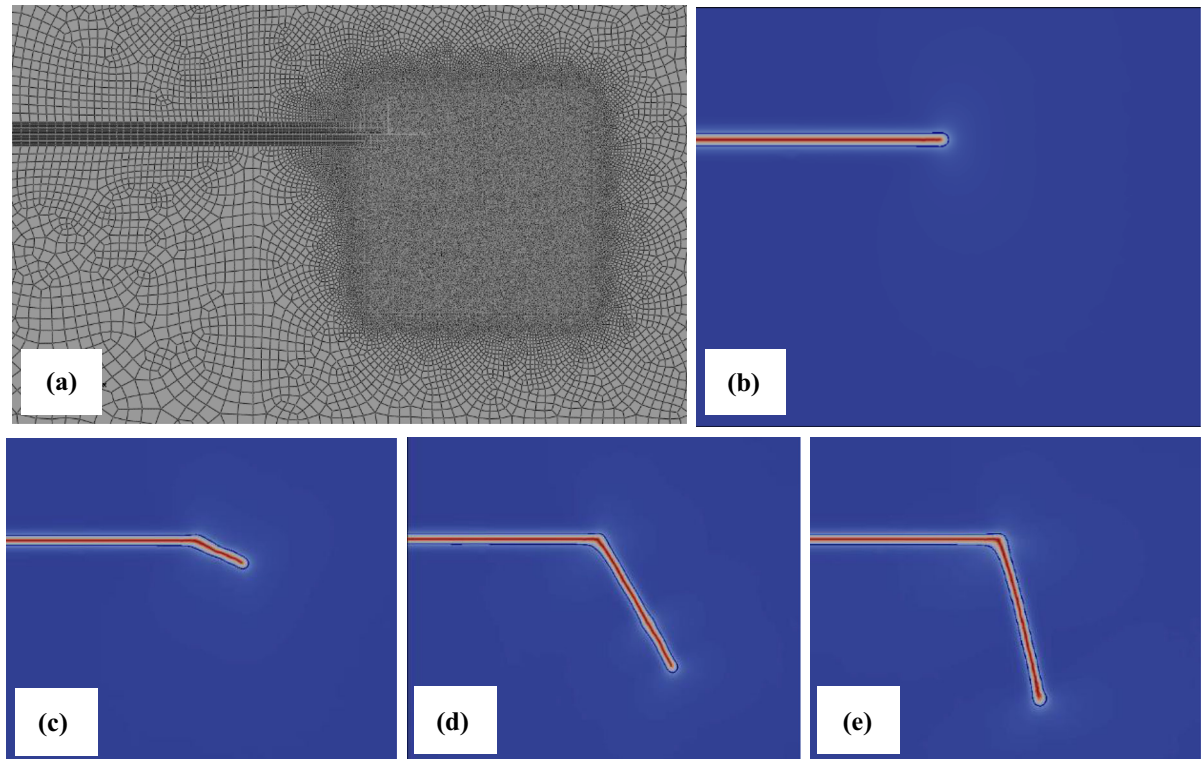


**Fig. 9** Mixed-mode I + II K-field loading simulations. The mesh has very fine regions along the initial crack line and in the rectangular area ahead of the crack front as indicated in (a). **b** Shows a crack path under pure mode I loading to form

a natural crack; this crack was used as the initial crack in subsequent simulations for mixed mode I + II. **c–e** The crack paths under mixed-mode I + II and pure mode II loading with the ratio  $K_{II}^{\infty}/K_I^{\infty} = 0.28, 1.12, \infty$

The maximum ERR criterion is the natural interpretation of Griffith's criterion which requires that the crack extend in the direction that minimizes the potential energy of the system (or maximizes the strain energy release rate for a material with constant fracture energy). Writing the energy release rate in terms of the stress intensity factors at the kinked crack, a mixed-mode I + II crack would extend in the direction  $\gamma_c$  along which

$$\frac{\partial G}{\partial \theta} = \frac{\partial}{\partial \theta} \left[ k_I^2(\theta) + k_{II}^2(\theta) \right] \Big|_{\theta=\gamma_c} = 0,$$

and  $\frac{1-\nu^2}{E} \left[ k_I^2(\gamma_c) + k_{II}^2(\gamma_c) \right] = G_c$       (26)

The variation of the crack kink angle with mode mixity and the critical combination of the mode I and mode II stress intensity factors at failure are shown in Figs. 10 and 11 respectively for all three models. The critical conditions at which the phase field simulations indicate

extension of the mixed-mode crack are also marked in these figures. Crack initiation is identified in the phase-field simulations using a very simple criterion: since  $l_0$  sets the scale of the fracture, crack initiation is taken to occur when  $c < c_c = 0.75$  is attained at an element at a distance  $2l_0$  from the initial crack tip; the critical conditions at initiation and the corresponding crack kinking angle are also shown in Figs. 10 and 11. Clearly, the phase field simulations indicate good agreement with the expectations from either the PLS or the ERR.

## 5 Validation by comparison to experiments for mixed-mode I + II

Experimental validation of the phase-field model is explored using the compact tension geometry and its modification. The experiments on mode I and mixed mode I + II are performed to provide data for quantitative comparison with simulations of the global response

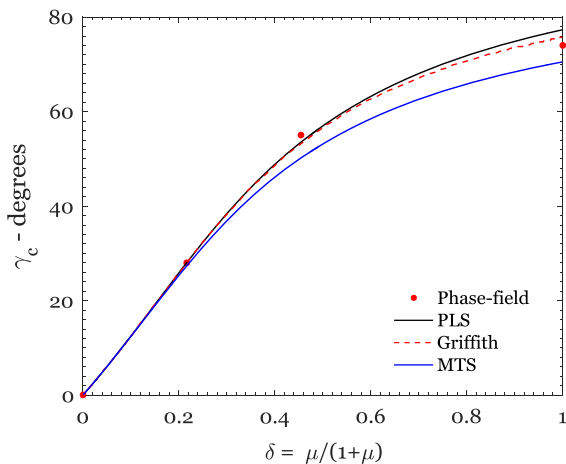


**Fig. 10** Comparison of the crack kink angle prediction from the phase-field model simulation results with the analytical solution for different crack initiation criteria for mixed-mode I+II loading (Note  $\mu = K_{II}^\infty / K_I^\infty$ )

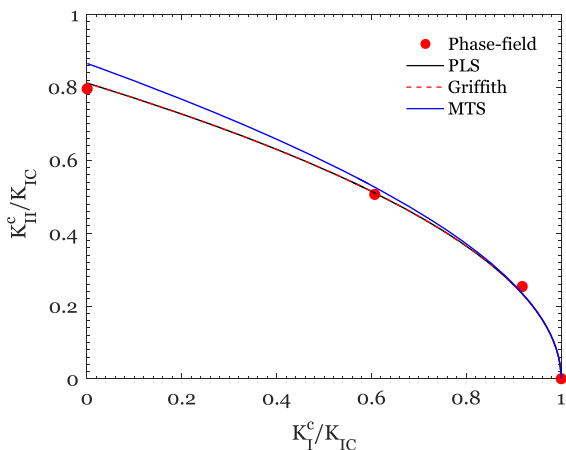


**Fig. 11** Comparison of critical combination of mode I and II SIFs between phase-field model simulation results and the analytical results for different crack initiation criteria for mixed-mode I + II loading

of the specimen as well as the exact evolution of the crack tip with loading.

### 5.1 Specimen geometry, material properties and experimental procedure

All the specimens were machined from the same sheet of polymethylmethacrylate (PMMA). The elastic modulus and Poisson's ratio were determined directly from

a tensile test; this test was performed on a “dog-bone” type specimen in an Instron Model 5582 universal testing machine, at a nominal strain rate of  $10^{-5} \text{ s}^{-1}$ . In addition to monitoring the global load with a load cell, the method of digital image correlation (DIC) was used to monitor the development of major and minor strains as a function of the global deformation, while still within the linear elastic regime; the specimen was not tested to failure. The resulting data was processed to determine the modulus of elasticity and the Poisson's ratio:  $E = 2.98 \text{ GPa}$  and  $\nu = 0.35$ ; this specimen used for calibration was extracted from a specimen on which a fracture test had been performed previously, ensuring that these values are appropriate for the same material.

The fracture energy was determined using a standard compact tension specimen geometry shown in Fig. 12a. The specimens tested have the dimensions  $W = 50.8 \text{ mm}$  and  $t = 3.0 \text{ mm}$ . Special attention was devoted to making a very sharp natural crack in front of the machined V-notch. A sharp, thin razor blade was mounted on an aluminum rod that was guided to move only in the vertical direction. The razor blade was then brought to contact with the tip of the V-notch; the aluminum rod was impacted with a hammer in order to wedge the razor blade into the V-notch and generate a natural crack. This technique produces a natural sharp crack ahead of the razor blade; this process produces a more reliable sharp crack in polymers than a fatigue cracking process; still, the crack front exhibits some curvature, and the crack surface exhibits roughness that were then characterized quantitatively after the crack growth test. The experimental setup used for the fracture toughness test is shown in Fig. 12b. The experiments were performed under displacement control in an Instron Model 5582 testing machine at a cross-head rate of  $4 \times 10^{-4} \text{ mm/s}$ . The load vs load-point displacement was monitored. In addition, the DIC technique was used to determine accurately the crack opening displacement (COD) at the load line, and to track the position of the crack front. Two cameras facing the specimen plane were used to capture the images of the areas used for calculating COD and tracking crack front location. These images were analyzed using the ARAMIS™ software. The crack front location at each time step was identified based on the highly localized strain values in the vicinity of the crack tip. The COD was also computed from the result of image analysis. Then time correla-

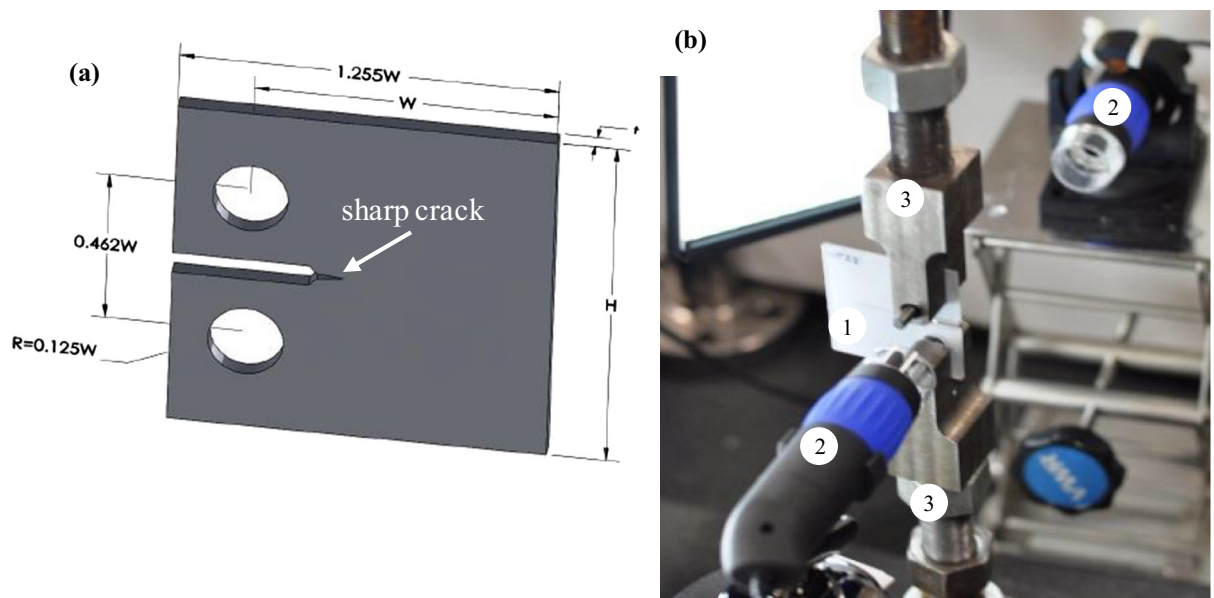
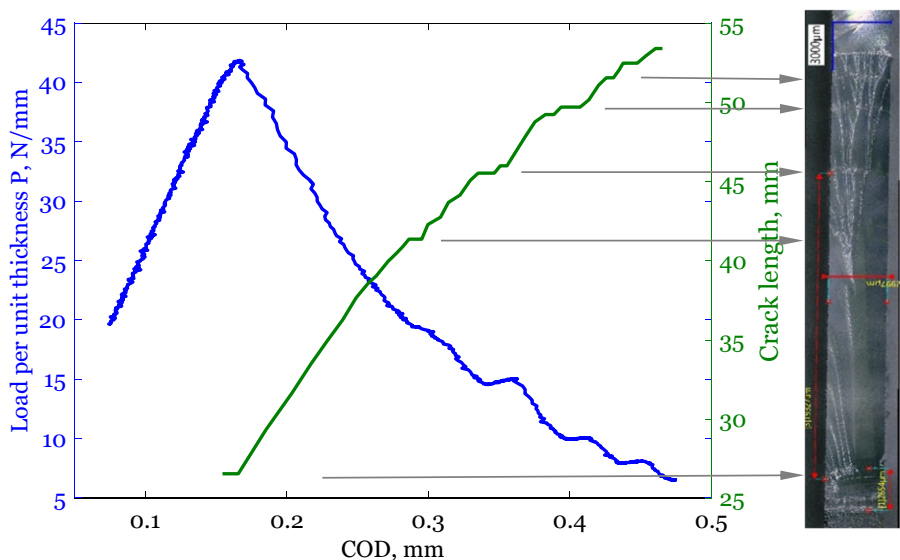


**Fig. 12** **a** Shows a sketch a compact tension specimen. The V-notch tip is located at  $0.45W$ ; and the wedge impact generated a sharp crack which has the length of  $a$  from the V-notch tip. **b** Shows the experimental setup: **1** specimen, **2** cameras, **3** loading grips

**Fig. 13** Load and crack length versus crack opening displacement (COD) for specimen CT\_24. The micrograph of the fracture surface indicates that the crack stopped many times along the path due to the local variation in fracture toughness; these arrest points are identified by the arrows



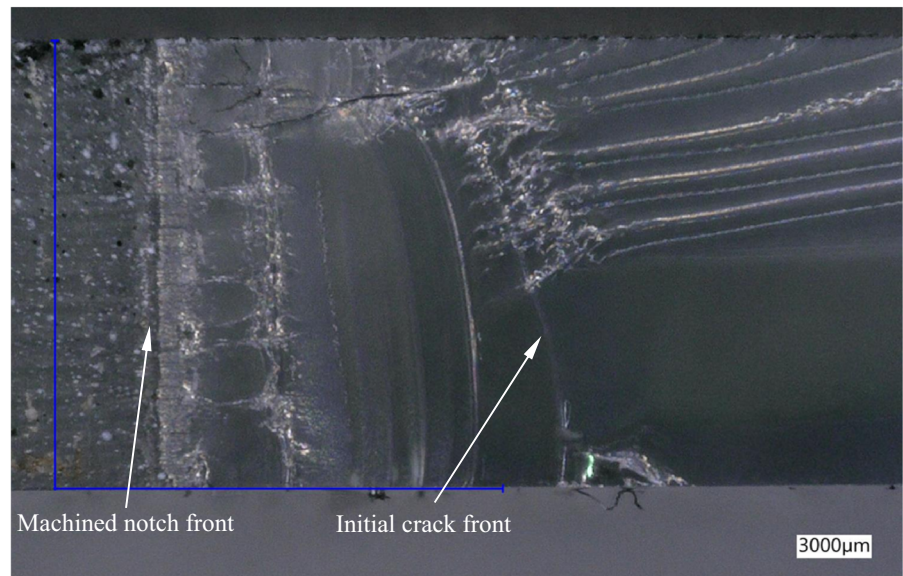
tion between image time sequence and loading time sequence was used to find the COD for each load step.

## 5.2 Experimental results: Mode I

Two sets of experiments were performed under mode I loading conditions: in the first set of experiments (spec-

imens CT\_21, CT\_22 and CT\_24), the cracks were allowed to grow until they almost broke through the free surface, while in the second set of experiments (specimens CT\_31, CT\_32 and CT\_33), they were allowed to grow only a short distance from the initial location. The plots of the load and crack length vs. COD for test CT\_24 are shown in Fig. 13; a micrograph of the fracture surface is also shown to the right of the plots, scaled appropriately. The load-COD response is lin-

**Fig. 14** Micrograph of the fracture surface of specimen CT\_24. The initial crack front generated by razor blade impact was not straight. The fracture surface exhibits many striations as the crack propagated; these are due to the fracture surface roughness generated by heterogeneity of the material and the details of the fracture process. The roughness, on the order of  $40 \mu\text{m}$ , is evidence of differences in the fracture process at different locations along the crack front



ear almost up to the point of the peak load while the crack remains stationary. Measurable crack extension begins as the COD reaches a value of  $0.163 \text{ mm}$ ; under the steady motion of the cross-head, the crack continues to grow, and the load begins to drop as the specimen compliance increases. At several points along the crack path, the crack stopped growing for brief periods, while both the COD and the load increased until the crack restarted its growth. Corresponding to each one of these arrest-reinitiation events, a residual mark was left on the fracture surface at the location identified in Fig. 13 by the arrows. A higher magnification image of the region near the initial crack for specimen CT\_24 is shown in Fig. 14. It should be noted that the crack front is curved along the thickness direction and further that the fracture surface is quite rough on one side and grows with a smoother surface on the other side. The upshot of these observations is that the response observed will exhibit some scatter. Similar observations/measurements were obtained from the two sets of experiments indicated above; the collection of these results will provide the basis for identifying the “nominal” behavior of this material. The load vs COD variation and the crack length vs COD variation from the collection of these experiments are shown in Fig. 15. The initial compliances are different for each specimen since the specimens have different initial crack lengths  $a$ . There was also some scatter of the critical load at which crack initiation occurred. For example, even though two pairs of specimens CT\_21 and CT\_31,

CT\_22 and CT\_24 had approximately the same initial crack length, their critical loads differ from each other by about 20%; this can be attributed to differences in the initial crack bluntness, curvature of the crack front in the thickness direction, and other “qualities” of the crack tip that influence the fracture process as pointed out for specimen CT\_24. These results point out that one should not rely on the critical load for an accurate calibration of the fracture toughness. On the other hand, as the crack grows further, the surface appears to be more uniform, and establishes self-similar crack growth from the perspective of the fracture process; the load vs. COD curves for most of the specimens seem to converge in this range, with only minor fluctuations.

Taking the above observations into account, the fracture toughness of the tested specimens was calibrated by fitting the part of the load-COD from the experimental data that corresponds to continued growth. Both the handbook solution (Murakami et al. 1987) and a J-integral calculation from the commercial software ABAQUS were used to determine the stress intensity factor as a function of crack length; the fracture toughness was then estimated to be  $K_{IC} = 0.98 \text{ MPa.m}^{1/2}$ . The load-COD curve determined based on this value of fracture toughness is shown in Fig. 15 as a thick black line; it can be seen to pass through the scattered data quite well; rigorous statistical measures have not been used in estimating the fracture toughness, although this poses no difficulties in principle. The corresponding fracture energy was calculated to be

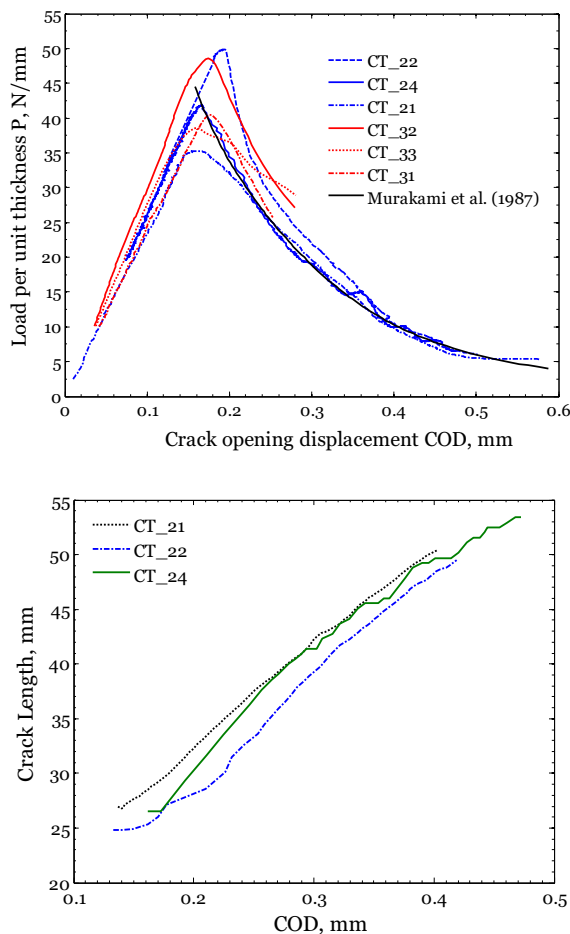


**Fig. 15** Load versus COD and crack position versus COD for the mode I tests using compact tension geometry

$G_c = (1 - \nu^2) K_{IC}^2 / E = 0.285 \text{ kJ/m}^2$ . The values of the fracture toughness and fracture energy are within the range commonly reported for this material.

### 5.3 Experimental results: Mixed-mode I + II Loading

Mixed-mode I + II loading was produced in the same CT specimen geometry used in the “mode I loading” by introducing a circular hole ahead of the crack line as indicated in Fig. 16. First, a sharp crack was created by impacting a thin razor blade as in “mode I loading” case. Next, these specimens were loaded to grow the short initial mode I natural cracks. Then, an end mill was used to drill a circular hole at the desired location ahead of the crack path. The mixed-mode I + II state was varied by changing the location of the circular hole

relative to the crack. The initial crack lengths of the specimens used in these experiments are in the order of  $a \sim 12 - 14 \text{ mm}$  (these specimens were marked as CT\_31, CT\_32 and CT\_33; and they were also used for mode I calibration experiments in the previous section). The load-COD curves for the initial mode I stage of the loading are shown in Fig. 17b, identified as Step 1, while the load-COD responses of the same specimens after the hole was introduced and reloaded again in mixed modes I + II are identified as Step 2. The crack paths are shown in Fig. 17a.<sup>2</sup> Due to the effect of the hole, the cracks started growing at a lower load level compared to their earlier state in the specimens without the hole; due to the asymmetry introduced by the hole, the crack path deviates from the line of symmetry and approaches the hole by gradually turning towards the hole. The specimens CT\_31 and CT\_32 show similar load-COD responses and crack paths. Linear elastic solution of this problem could be approached through finite element or boundary element techniques, but this is not pursued; instead, we will use these as experimental results for validation of the phase-field simulations.

### 5.4 Comparison between experimental and phase-field simulation results

The mode I and mixed-mode I + II validation problems considered in Sects. 5.2 and 5.3 are 2D problems. The effect of the free surface on the crack front shape is small. Thus we adopted a plane strain calculation strategy for these problems. The displacement boundary conditions were applied at two points in the pin-hole: the vertical and horizontal nodal displacement components were prescribed.

#### 5.4.1 Comparison of simulations and experiments for Mode I loading

The finite element computational mesh was created based on the geometry of specimen CT\_24 (see Fig. 18)

<sup>2</sup> Curving vs kinking: The crack paths shown in Fig. 17a are all smooth curves; when the crack was far from the hole, mode II loading increases gradually from zero as the crack approaches the vicinity of the hole. In contrast, if the hole was drilled close to the initial crack, the loading generated a finite jump in mode II loading, and hence the crack initiated with a kink relative to the initial crack. Here, we have only analyzed those experiments that involved a smooth curving of the crack.

**Fig. 16** Geometry for a modified compact tension specimen with crack under mixed-mode I + II loading (left), and the final crack path for specimen CT\_31 (right)

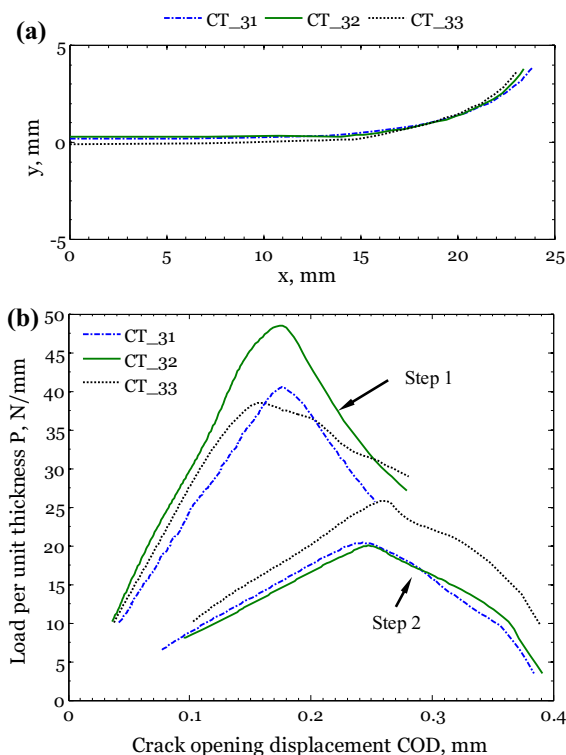
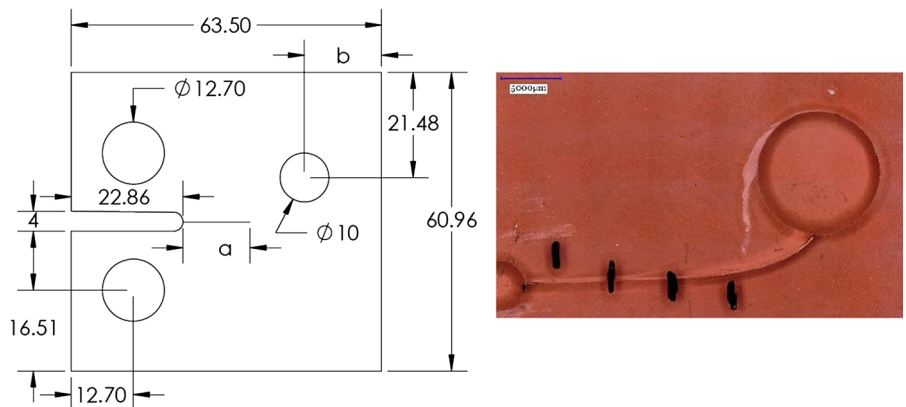
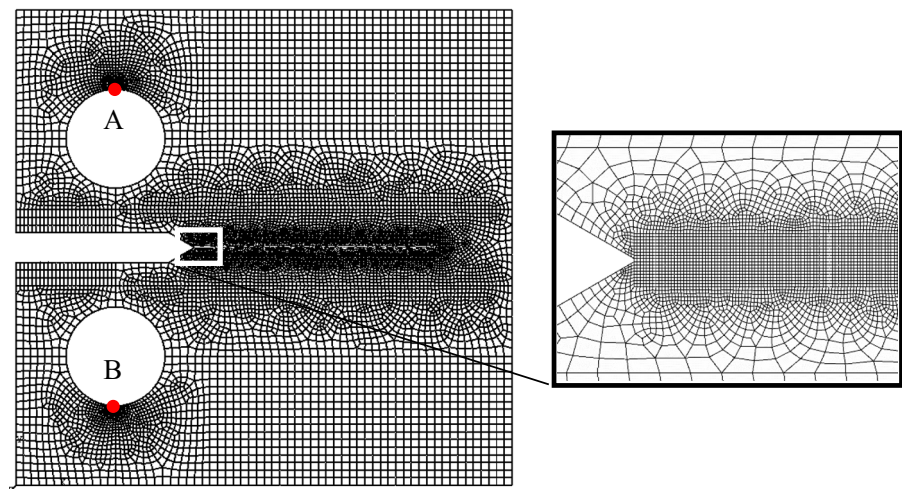


**Fig. 17** Experimental results for mixed-mode I + II loading of specimens CT\_31, CT\_32 and CT\_33 with the initial straight cracks of length  $a = 13.47, 14.01, 12.98$  mm, respectively (the hole is located at  $b = 15.80$  mm). **a** The crack paths are plotted (the reference is taken to be the tip of the notch). **b** Load versus COD. First, the CT specimens were loaded to grow the straight mode I cracks of initial length  $a$  (family of curves labeled Step 1). Then, a hole was introduced into these specimens and they were reloaded (family of curves labeled Step 2)

with the initial crack length measured from the fracture surface. This mesh contains approximately 52,000 hexahedral elements with only one element in the thickness

direction with periodic boundary conditions imposed in this direction. The region that contains the expected path of the crack was meshed with very small element size of  $h = l_0/4$ , where  $l_0 = 100 \mu\text{m}$ ; both structured and unstructured mesh geometries were used in order to evaluate potential mesh effects on the crack path. The initial natural crack which was generated by the razor blade impact in the experiment is modeled by prescribing the phase-field nodal value to zero for nodes on the central line element within the initial crack length. The simulation was performed by incrementing the displacements at the nodes corresponding to the loading pins in the experiment (identified as points A and B in Fig. 18). This simulation was run on 80 processors; and it took about 2 h to complete (each staggered iteration took about 500 iterations to converge). The simulation results and comparison with experimental data for specimen CT\_24 are shown in Fig. 19, where the load-COD variation as well as the crack length vs COD variation are shown. The crack “tip” in the phase-field simulation was identified as the farthest location from the notch, along the initial crack line at which the phase field parameter reached its critical value  $c_c$ . The load-COD curve from the simulation matches the experimental result very well, with an initial elastic response of a stationary crack up to a COD of about 0.16 mm and then followed by a drop of the load as the crack begins to grow. Crack growth followed the line of symmetry for this mode I loading condition; the load-COD curves from both simulation and experiment agree well with each other during this stage. Considering the fact that repeated experiments on nominally the same geometry resulted in crack initiation at different critical levels, (mainly as a result of possible bluntness and other irregularities of the crack tip) both load-COD and crack

**Fig. 18** Mesh discretization for specimen CT\_24. The smallest elements along the crack path have a size of  $25 \mu\text{m}$ . A magnified view of the fine mesh region is shown to the right



length-COD plots from simulation result fall inside the experimental data scatter. This indicates that the chosen length for the phase-field model –  $l_0 = 100 \mu\text{m}$  is appropriate for the characterization of mode I fracture in this material for the particular specimen dimensions.

#### 5.4.2 Comparison of simulations and experiments for mixed-mode I + II loading

Simulations associated with the specimens reported in the experimental section for mixed-mode I + II loading are explored. The initial crack geometry of specimen CT\_31 was used in these simulations. The initial straight crack of length  $a$  is modeled as follows: double nodes are used within the length of  $(a - 2l_0)$ ; the length  $2l_0$  ahead of these double nodes are meshed with a line of elements whose phase-field nodal values are prescribed to be zero. The mesh effect was also explored in these simulations: we used a structured mesh (with  $h = l_0/4$ ) and two unstructured meshes (with both  $h = l_0/4$  and  $h = l_0/16$ ) in the area around the expected path of the crack.

The results for the simulation associated with specimen CT\_31 are presented in Figs. 20 and 21. Figure 20a shows an overall view of the crack path as it approaches the hole. Figure 20b shows the crack path comparison for the simulations using structured and unstructured meshes, but at a greater magnification. The mesh effect manifests itself in the deviation in crack paths as well as load-COD curves (see Fig. 21). The crack path from structured mesh exhibits a stair step curve, while it is smoother in the case of unstructured mesh. This implies that the unstructured mesh is preferable

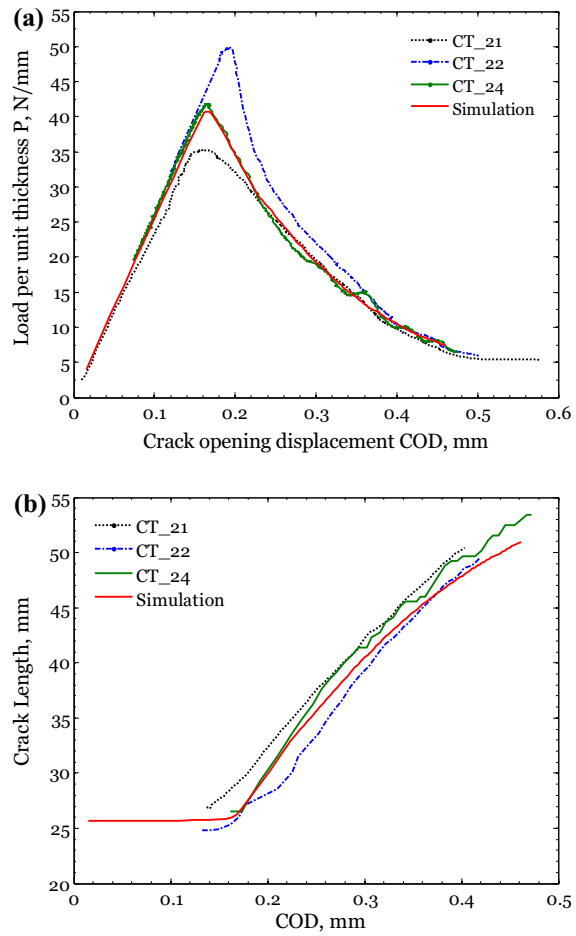


**Fig. 19** Comparison between experimental results and simulations for specimen CT\_24. The average initial crack length for specimen CT\_24 was measured accurately from the fracture surface information and used in these simulations. **a** Load versus COD. **b** Crack length versus COD

**Fig. 20** **a** The crack path for the simulation based on the geometry of specimen CT\_31 using a uniform mesh. **b** The iso-volume plots of the phase-field variable between 0 and 0.01 for the structured mesh and unstructured mesh

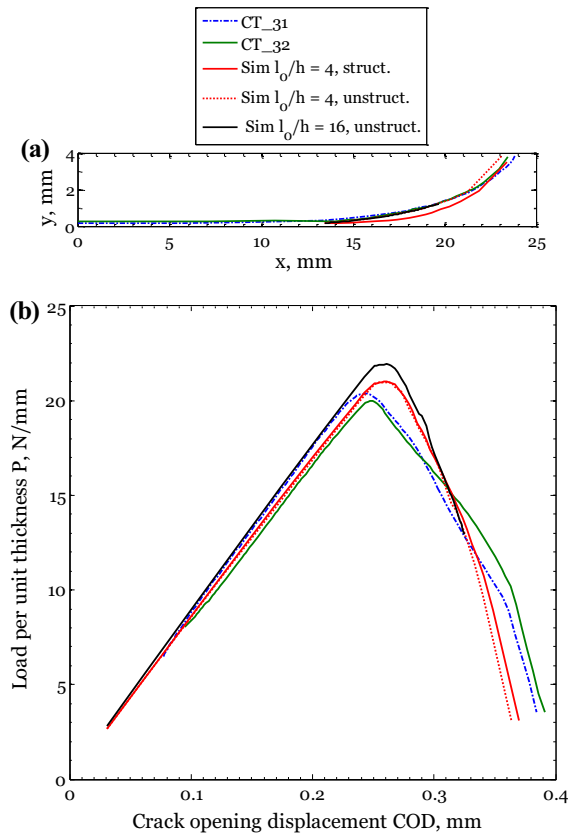
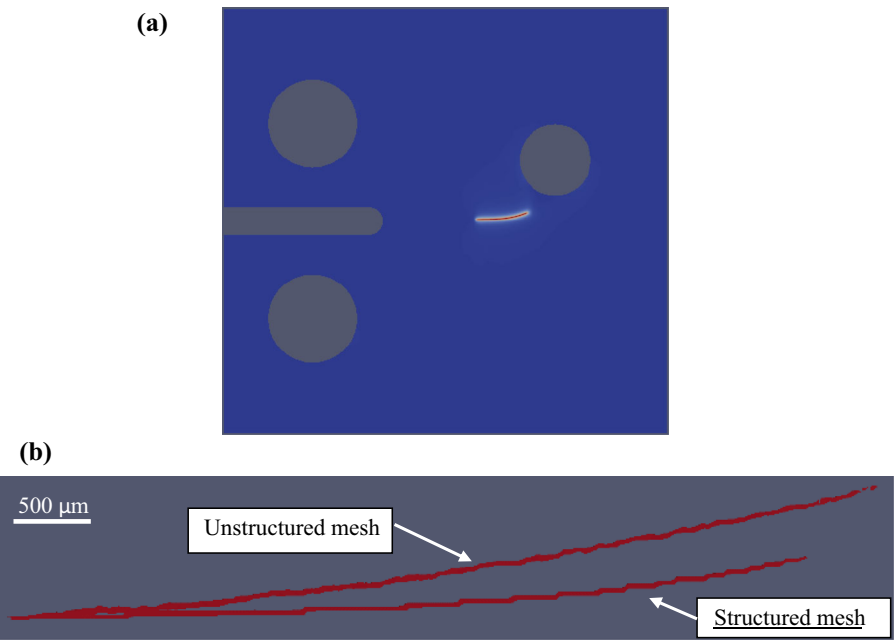


**Fig. 21** Comparison between experimental results and the simulation with the geometry based on the specimen CT\_31

since it can represent the curvature of the crack path under mixed-mode I + II better. The crack paths for the unstructured meshes size of  $h = l_0/16$  and  $h = l_0/4$  are not significantly different, but the load-COD curves are not the same and have a small deviation. This can be explained by the fact that the fracture energy release rate amplification formula proposed by Bourdin et al. (2008) is not an exact formula but an approximation. The smaller mesh size simulation gives a closer load-COD behavior for the elastic portion where the crack has not grown. For both meshes, the critical loads are higher in comparison to the experimental data. The simulations using unstructured meshes can predict the crack path very close to the experimental data, but the load-COD curves still exhibit discrepancy. The discrepancy may be caused by the difference in the boundary conditions enforced in the simulation and the actual boundary conditions used in the experiments: the pin supports for the two pin-holes must be modeled as contact boundary condition in the simulations, but the current version of our code is not able to handle this kind of boundary conditions. For the case of mode I loading discussed in previous section, the crack grows along the surface of symmetry, thus the specimen rotation is small. In the case of mixed-mode I + II the crack goes off the plane of symmetry which causes the rotation of specimens. The boundary conditions used in our code prevent this rotation; and this causes some discrepancy

to occur. We suspect that if the boundary conditions are modeled exactly as those used in the experiments, the phase-field simulation may predict the crack path and structure response under mixed-mode I + II loading more accurately.

Based on the comparisons explored in these sections, it can be stated that the phase-field model provides an acceptable simulation for the global response of the structure, as well as the growth of the crack for the in-plane mixed-mode I + II problems. Some details of the local field, in the vicinity of the crack over lengths on the order of a few hundred  $l_0$  are likely to be incorrect as a result of the approximation of the fracture process.

## 6 Conclusion

A phase-field model of fracture has been implemented in a parallel simulation framework for simulation of three-dimensional linear-elastic fracture problems. The numerical code has been verified for stationary crack problems by comparison of the crack opening displacement with the analytical linear elastic singular solution and the Dugdale–Barenblatt cohesive model solution. Based on these exercises, it was determined that the scale of the fracture process zone is on the order of  $8l_0$ , and hence the phase-field solutions will deviate from the elastic solutions for a length on the order of  $\sim 100l_0$ . Next, the crack opening displacement calculations from the phase-field model were compared for a problem of a microcrack interacting with a macrocrack. Finally, mixed-mode I + II crack growth was simulated using the phase-field model and the results for the crack kink angle and the stress-intensity levels at initiation were compared with models based on the maximum tangential stress, maximum energy release rate criterion, and the principle of local symmetry. All the verification exercises generated excellent agreement with the analytical solutions.

Validation of the model was sought through comparison to experiments. Experiments were performed under mode I and mixed-mode loading conditions on compact tension specimens in a thermoplastic polymer, polymethylmethacrylate (PMMA). The materials properties were obtained through direct calibration on the same stock of material. While the elastic response was quite repeatable, noticeable scatter was observed in the case of the fracture tests. Calibration of the frac-

ture energy (or fracture toughness) was obtained by fitting the mean trend over multiple experiments, when considering a steadily growing crack. The mode I and mixed-mode I + II experiments were then simulated using the phase-field code. Very good agreement was obtained when comparing the load vs crack opening displacement response as well as the crack position vs the crack opening displacement response; crack paths were also well-predicted by the phase field model. This validated phase-field code will be used in a future contribution to examine three dimensional crack problems under mixed-mode I + III loading.

**Acknowledgements** Parts of this work were performed during the course of an investigation into failure under a related research program funded by the Army Research Office (Grant Number: W911NF-13-1-0220). The computations performed as part of this work were supported by a generous allocation of time by the Texas Advanced Computing Center. The authors gratefully acknowledge this support.

## References

- Ambati M, Gerasimov T, De Lorenzis L (2015) A review on phase-field models of brittle fracture and a new fast hybrid formulation. *Comput Mech* 55:383–405
- Ambrosio L, Tortorelli VM (1990) Approximation of functionals depending on jumps by elliptic functionals via  $\Gamma$ -convergence. *Commun Pure Appl Math* 43(8):999–1036
- Ambrosio L, Tortorelli VM (1992) On the approximation of free discontinuity problems. *Boll Un Mat Ital B* (7) 6(1):105–123
- Amor H, Marigo JJ, Maurini C (2009) Regularized formulation of the variational brittle fracture with unilateral contact: numerical experiments. *J Mech Phys Solids* 57:1209–1229
- Balay S et al (2014) PETSc users manual. ANL-95/11—Revision 3.5. Argonne National Laboratory, Chicago
- Borden MJ et al (2012) A phase-field description of dynamic brittle fracture. *Comput Methods Appl Mech Eng* 217:77–95
- Bourdin B (1999) Image segmentation with a finite element method. *M2AN Math Model Numer Anal* 33(2):229–244
- Bourdin B, Francfort GA, Marigo JJ (2000) Numerical experiments in revisited brittle fracture. *J Mech Phys Solids* 48(4):797–826
- Bourdin B, Francfort GA, Marigo J (2008) The variational approach to fracture. *J Elast* 91:5–148
- Braides A (1998) Approximation of free-discontinuity problems. Number 1694 in Lecture Notes in Mathematics. Springer, Berlin
- Chambolle A (2004) An approximation result for special functions with bounded variations. *J Math Pure Appl* 83:929–954 2004
- Chambolle A (2005) Addendum to an approximation result for special functions with bounded deformation [J Math Pure

- Appl (9) 83 (7) (2004) 929–954]: the n-dimensional case. *J Math Pure Appl* 84:137–145
- Erdogan F, Sih GC (1963) On the crack extension in plates under plane loading and transverse shear. *J Basic Eng* 85:519–525
- Giacomini A (2005) Ambrosio–Tortorelli approximation of quasi-static evolution of brittle fractures. *Calc Var Partial Differ Equ* 22(2):129–172
- Goldstein RV, Salganik RL (1974) Brittle fracture of solids with arbitrary cracks. *Int J Fract* 10:507–523
- Karma A, Kessler DA, Levine H (2001) Phase-field model of mode III dynamic fracture. *Phys Rev Lett* 87:045501
- Karypis G, Kumar V (1999) A fast and high quality multilevel scheme for partitioning irregular graphs. *SIAM J Sci Comput* 20:359–392
- Leblond JB (1999) Crack paths in three-dimensional elastic solids. I: two-term expansion of the stress intensity factors—application to crack path stability in hydraulic fracturing. *Int J Solids Struct* 36:79–103
- Miehe C, Hofacker M, Welschinger F (2010) A phase field model for rate-independent crack propagation: Robust algorithmic implementation based on operator splits. *Comput Methods Appl Mech Eng* 199:2765–2778
- Murakami Y et al (1987) Stress intensity factors handbook, vol 1. Pergamon Press, New York
- Ortiz M (1985) A constitutive theory for the inelastic behavior of concrete. *Mech Mater* 4:67–93
- Pham K, Amor H, Marigo JJ, Maurini C (2011) Gradient damage models and their use to approximate brittle fracture. *Int J Damage Mech* 20(4, SI):618–652
- Pham K, Marigo JJ, Maurini C (2011) The issues of the uniqueness and the stability of the homogeneous response in uniaxial tests with gradient damage models. *J Mech Phys Solids* 59(6):1163–1190
- Rubinstein AA (1985) Macrocrack interaction with semi-infinite microcrack array. *Int J Fract* 27:113–119